Visualization of Charge Migration in Conductive Polymers via Time-Resolved Electrostatic Force Microscopy

doi: https://doi.org/10.1021/acs.jpca.9b12017

Visualization of Charge Migration in Conductive Polymers via Time-Resolved Electrostatic Force Microscopy

Kentaro Kajimoto, Kento Araki, Yuki Usami, Hiroshi Ohoyama, Takuya Matsumoto*

Department of Chemistry, Graduate School of Science, Osaka University, 1-1 Machikaneyama-cho, Toyonaka, Osaka, Japan.

matsumoto-t@chem.sci.osaka-u.ac.jp

Abstract

Charge dynamics play an important role in numerous natural phenomena and artificial devices, and tracking charge migration and recombination is crucial for understanding the mechanism and function of systems involving charge transfer. Tip-synchronized pump–probe electrostatic force microscopy simultaneously permits highly sensitive detection, microsecond time resolution, and nanoscale spatial resolution, where the spatial distribution in static measurement (usual EFM) reflects differences in the carrier density and the time evolution reveals the surface carrier mobility. By using this method, carrier injection and ejection in SPAN thin films were visualized. Comparison of tr-EFM results of SPAN thin films with different doping levels revealed the individual differences in carrier density and mobility.

1. Introduction

The micro- or nanoscale generation, migration, and recombination of local charges (collectively referred to as charge dynamics) play essential roles in many natural and artificial systems or phenomena, including the brain, light harvesting, photosynthesis, catalysis, photovoltaic devices, and field-effect transistors.[1–7] Charge tracking is intrinsically important for understanding the fundamental characteristics of these systems as well as the fabrication of functional materials and devices.

To date, the early processes of photoexcited charge dynamics have been extensively investigated using nonlinear optical methods based on time-resolved spectroscopy, which has afforded an electronic explanation for charge generation and separation. However, the subsequent charge behavior (migration and recombination) that dominates the exploitation and application of the separated and/or injected charges has not yet been elucidated. To accomplish this, techniques are needed that have high spatial resolution beyond the optical diffraction limit.[8]

Scanning probe microscopy (SPM) methods are effective because they are highly sensitive and their spatial resolution can extend to the level of individual atoms and molecules. However, SPM detection systems are slow to operate. Although high-speed SPM platforms equipped with specially tuned feedback systems can be used to observe millisecond phenomena, including crystal growth and protein motions,[9–11] charge dynamics require considerably faster observations. Time resolution in scanning tunneling microscopy (STM) was initially reported in 1990 by Hamers and Cahill, who applied the pump–probe method.[12] Subsequently, Shigekawa and co-workers achieved femtosecond time resolution using terahertz pump–probe

STM.[13,14] Although these approaches simultaneously realized fast time resolution and nanoscale spatial resolution, the samples were limited to semiconductors because the STM measurement required a nonlinear tunneling current. Consequently, the observable phenomena were limited to the modulated densities of states and work functions. For tracking charge migration and recombination, the charge should be directly detected from the functional materials typically used in device applications, such as insulators, wide-bandgap semiconductors, and poorly conducting surfaces.

Electrostatic force microscopy (EFM), which is based on atomic force microscopy, can be used to probe isolated local charges[15, 16] and single electrons.[17] This technique has previously been used to examine nanoscale charge behavior in natural systems and artificial devices, including inorganic semiconductors, catalysts, batteries, organic field-effect transistors, and organic photovoltaics.[18–24] These literature reports have demonstrated the power and utility of EFM for time-resolved charge tracking.

Time-resolved EFM (tr-EFM)[25] has been accomplished via three main approaches. In the first approach, time resolution is achieved by completely recording and analyzing the cantilever motion. This method is suitable for a wide range of temporal scales down to submicrosecond resolution, although it does require post-processing. Ginger and co-workers utilized the Hilbert transform,[26, 27] whereas Collins et al. proposed the use of Kelvin probe force microscopy with fast free force reconstruction by filtering and deconvoluting the G mode.[28]

In the second approach, Grutter and co-workers reported that the time resolution can be achieved by a two-pulse method through a nonlinear response to double-pulse excitation similar to that of time-resolved STM.[29] This method permits picosecond time resolution without being dependent on the cantilever motion. However, isolated charges are difficult to probe because the nonlinear response arises from the potential shift due to the local carrier density in semiconductor bands. Furthermore, microsecond time resolution is sufficient for observing the charge transfer, migration, and recombination processes because the tunneling and hopping probabilities result in slower dynamics that occur on longer than submicrosecond timescales.[30]

The third approach is another pump–probe method in which the pump generates and injects charge pulses, which are detected using the probe as a pulsed electrostatic force. This method can be used to detect isolated charges without a nonlinear response. In voltage pump–probe experiments, Eng and co-workers reported microsecond time-resolved EFM images of organic field-effect transistors.[31, 32] However, this method inevitably introduces unrelated tip motions into the pump–probe detection, such that the tip–sample distance always fluctuates at the moment of the probe pulse. This uncertainty limits the sensitivity and spatial resolution associated with this method and causes experimental fluctuation of the external electric field.

Therefore, we previously proposed a tip-synchronized tr-EFM method involving the generation of pump pulses with a constant phase of cantilever vibration.[33] In this method, the charge detection at the tip position closest to the sample surface corresponds to the probe detection in the pump–probe framework, improving the sensitivity and spatial resolution compared with standard EFM methods. Using a similar approach, Marohn and co-workers employed phase-kick EFM for time-resolved electrostatic force detection.[34] Recently,

we were able to obtain a video showing photoexcited carrier migration on an organic photovoltaic device with a time resolution of 0.3 μs and sensitivity of 0.3 Hz.[35]

In this study, tip synchronization is extended to dual-bias pump–probe measurements. This extension improves the sensitivity and resolution by utilizing only the condition of the closest tip–sample distance, enabling observations of the charge behavior on poorly conducting materials, particularly conductive polymers, which are being actively researched as innovative materials for manufacturing flexible displays, photovoltaics, and thermoelectric conversion systems. In such materials, the localized charge carriers in disordered and inhomogeneous structures are transported by hopping between metallic sites.[36] Therefore, the ability to visualize the charge transport on conductive polymers would clarify the behavior and pathways of carriers in organic electronics and thermoelectronics. As a self-doped polymer, we employ sulfonated polyaniline (SPAN, Scheme 1), which exhibits high solubility in water and high conductivity conferred by the self-doped sulfonic acid.[37] The conductivity of SPAN can be controlled by adjusting the pH while preparing the SPAN thin film.[38] Furthermore, the carrier injection and ejection processes in SPAN thin films with various levels of doping are observed at submicrosecond and nanoscale resolutions.

2. Experimental

Si wafers with a thermally grown oxide layer of 300 nm thickness were used as substrates. Each substrate surface was ultrasonically cleaned in acetone for 15 min, dried under dry N_2 gas, and subjected to UV/O_3 cleaning for 1 h. SPAN thin films were fabricated on the surface by dropping solutions of 5×10^{-3} wt% SPAN (aquaPASS, Mitsubishi Rayon, Japan) with or without NaOH followed by air drying at room temperature. A pair of top-contact Au electrodes of 50 nm thickness were then patterned on the SPAN layer via thermal deposition to serve as the drain and source electrodes.

The doping levels of SPAN afforded by the SPAN solutions with various NaOH concentrations (0–1.0×10^{-3} M) were measured from the UV–vis absorption spectra obtained using a spectrophotometer (UV-1800, Shimadzu). The appropriate doping level for the tr-EFM measurements was determined from the four-terminal *I*–*V* characteristics of SPAN thin films measured using a source meter (2636B, Keithley) with a multi-probe station (Apollowave) under vacuum ($<10^{-3}$ Pa) at room temperature. Figure 1a presents the UV–vis spectra of 5×10^{-3} wt% SPAN solutions containing various concentrations of NaOH. As the NaOH concentration increased, the intensities of the peaks corresponding to the polaron band (approximately 470 nm) and extended coil (near-infrared) decreased, while that of the peak corresponding to the localized polaron band (750–900 nm) increased, indicating the occurrence of deprotonation.[38] Judging from the *I*–*V* characteristics shown in Figure 1b, a NaOH concentration of 1.0×10^{-4} M afforded suitable conductivity for comparing doped and underdoped SPAN thin films. Four-terminal *I*–*V* measurements afforded the thin-film carrier densities of SPAN only and SPAN with NaOH as 1.8×10^{22} m^{-3} and 4.5×10^{21} m^{-3}, respectively, while impedance measurements provided the carrier mobilities of SPAN only and SPAN with NaOH as μ = 0.25 cm^2/Vs and 0.015 cm^2/Vs, respectively (the details are presented in supporting material S9).

Figure 2 presents a schematic depiction of the tr-EFM apparatus. The sample had a field-effect transistor structure. An external bias was applied to the drain electrode, while the source electrode and Si wafer were always grounded. The measurements were conducted using a commercially available SPM system (JSPM-4200, JEOL) fitted with improved electrical circuits to avoid pulse broadening and Pt/Ir-coated cantilevers with a spring constant of 42 N/m and resonant frequency of ca. 300 kHz (PPP-NCHPt-50, Nanoworld). SPM scanning was performed in the constant-amplitude feedback mode (tapping mode) to maintain a constant tip–sample distance and examine the sample topography. The cantilever was vibrated by self-excitation at its resonant frequency. The frequency shift was monitored using a phase-locked loop (PLL; OC4 station, Nanonis) to measure the attractive force resulting from the electrostatic interaction between the tip and sample. A detailed explanation of this combined amplitude modulation–frequency modulation mode has been described previously.[35] The tr-EFM experiments were conducted under vacuum ($<10^{-2}$ Pa) at room temperature.

Figure 3 shows the timing chart for the time-resolved measurements. The trigger signal was generated by cantilever vibration. The duration of the pump pulse V_d applied to the drain electrode was set to be sufficiently long (typically 11 μs) to attain saturation of the charge state in the SPAN layer and controlled to be an integer multiple of the cantilever oscillation period to avoid interference between the pump pulse and tip motion. During the pump–probe experiments, the probe pulse V_t applied to the tip (1 μs duration) was locked at the moment when the tip reached its closest position to the sample surface. The delay between the pump and probe pulses was controlled by a trigger signal before one cycle of cantilever oscillation. This method of delay control was considered to have sufficient accuracy because the value of the frequency shift was only several hertz, which is on the order of parts per million with respect to the resonant frequency (ca. 300 kHz). To achieve high detection sensitivity, on/off modulation of the probe pulse train was employed using a lock-in amplifier (LI5640, NF Corporation). To reduce the spike noise, a 3×3 median filter was used to obtain the tr-EFM images.

3. Results and Discussion

3.1. Tip synchronization during time-resolved EFM

Tip-synchronized tr-EFM requires phase synchronization of the pump–probe excitation and detection of the fluctuating cantilever vibration. The quadrant photodiode signal monitoring the cantilever motion is sufficient to determine the instantaneous frequency of the tip vibration, but it is insufficient for identifying the moment of the closest position of the tip to the surface owing to the phase delay originating from the limited response of the photodiode and subsequent circuit. For this reason, the actual phase delay was determined from a plot of the experimental frequency shift change as a function of phase delay. Figure 4a reveals a clear phase delay effect on the Au surface with a DC sample bias of $V_s = -4.0$ V and a probe pulse of $V_t = 4.0$ V with 1.0 μs duration, where the frequency shift reflecting the strength of the tip–sample attractive interaction changed periodically and exhibited a maximum value at $\theta_d = 212°$ for the closest tip–sample

distance.

Using this phase delay condition, the time-resolved electrostatic force on the Au sample surface with periodic sample bias was examined by plotting the frequency shift as a function of the timing of the probe pulse with and without tip synchronization, as shown in Figure 4b. In this plot, the shaded region indicates a sample with $V_s = -4$ V as the ON state and the non-shaded region a sample with $V_s = 0$ V as the OFF state. Without tip synchronization, the difference in the frequency shift between the ON and OFF states was approximately 5 Hz. Upon tip synchronization, this difference increased to approximately 10 Hz. As this experiment was conducted for a single fixed point on the Au film surface, the noise level was less than 2 Hz. However, as discussed later, the noise level in the experiments involving SPAN thin films typically exceeded 4 Hz. Accordingly, the tip-synchronization is crucial for the investigation of charge migration in low conducting materials.'

3.2. Time-resolved observation of charge dynamics on SPAN thin films

Pump–probe tr-EFM measurements with tip synchronization as described above were performed using a pump pulse of $V_d = -2$ V (11 μs duration) and a probe pulse of $V_t = 2$ V (1 μs duration). Figure 5b shows the transient processes of carrier charge injection to the SPAN thin film immediately after setting V_d to −2 V. In these data, t denotes representative time at the middle of probe pulse. The cross-sectional profiles of frequency shift were obtained as the average of line scans across the area between the drain and source electrodes. The bright regions indicating the presence of charges increased from the drain side and the cross-sectional profiles gradually approached a linear gradient as time elapsed.

Figure 5c presents tr-EFM images showing the time evolution of the discharge processes immediately after setting V_d to zero. The charges remained at the center of the SPAN thin film between the drain and source electrodes and gradually discharged over time.

We extracted the physical parameters for the charge dynamics from the tr-EFM results by comparison with the model calculations for the hopping model shown in Figure 6a and b. The details of this calculation are described in supporting material S4.

In the hopping model, carrier transport is dominated by the hopping barrier between electron trap sites. The effective barrier height decreases with increasing slope of external potential versus carrier density.[39] The results of model calculation reproduced well experimental section profiles in figure 5b and c. Figure 6a shows the product of the potential and carrier density obtained from the one-dimensional hopping site model described in supporting material S4. Comparison of the cross-sectional profiles shown in Figures 5a and 6a confirms that the carrier injection process (i.e., OFF state to ON state) was qualitatively reproduced.

By fitting the observed tr-EFM cross-sectional profiles using the model calculations, the carrier mobility μ was obtained as in the range of 0.65~0.016 cm^2/Vs from analysis of the variation in the carrier density distribution. This value was close to the value of 0.25 cm^2/Vs determined from the electrical properties of the thin films.

3.3. Charge dynamics of underdoped SPAN thin films

To determine the effect of the doping level on the charge behavior, untreated and NaOH-doped SPAN thin films were compared. The addition of NaOH is known to cause deprotonation of the SPAN imine moieties, thereby reducing the polaron density and inducing a conformational change from an expanded coil to a compact coil.[38] Consequently, NaOH addition leads to a decrease in conductivity.

Figure 7 presents tr-EFM images of SPAN thin films with and without NaOH. In the ON state, the potential of the SPAN thin film without NaOH reached the drain potential. In contrast, the SPAN thin film with NaOH exhibited discontinuity at the edge of the drain electrode and a valley at the edge of the source electrode. These results indicate that the carrier density of the SPAN thin film with NaOH was insufficient to generate potential along the drain–source potential difference, and the overall potential of the sample shifted due to floating behavior, suggesting a poor electrical connection between the film and electrode even in the ON state. In fact, the carrier density determined from thin-film measurements was 1.8×10^{22} m^{-3} for SPAN alone and 4.5×10^{21} m^{-3} for SPAN with NaOH. carrier density of SPAN with NaOH was inferior to that of SPAN alone. It is difficult to estimate absolute values of carrier density from EFM measurements. However, in the case of SPAN with NaOH, the detected electrostatic force dropped at the edge of the drain electrode because there were not enough carriers to follow the external bias. It is therefore reasonable to consider that a difference in the amount of carriers influenced the spatial distribution during tr-EFM.

After turning off V_d, the charge in the region adjacent to the drain electrode was discharged and that in the center region remained. This behavior can be clearly observed for the SPAN thin film without NaOH at 0.7 μs after turning off V_d. In contrast, for the sample with NaOH, such behavior was only slightly observed after 10.7 μs. This directly indicates that the carrier mobility of SPAN is considerably reduced by the addition of NaOH. Differences in carrier mobility were also clearly observed in the tr-EFM images obtained immediately after turning on V_d again. For the sample without NaOH, the potential increase occurred immediately from the edge of the drain electrode. In contrast, for the sample with NaOH, a potential valley remained at the edge of the electrodes. In the time-resolved measurement of the SPAN film with NaOH, a pump pulse was applied again prior to discharge of all of the injected carriers. Therefore, slow carriers that cannot follow this ON/OFF cycling act as an offset at any timing, and the region that changes between the ON and OFF states (corresponding to the appearance of the valley near the electrode) represents relatively fast carrier movement.

The carrier mobility in SPAN thin films with NaOH was also estimated by comparison of the results of tr-EFM and the model calculations described above. The obtained carrier mobility for SPAN thin films with NaOH was obtained as in the range of 0.076~0.0019 cm^2/Vs. Therefore, in terms of the thin-film properties, NaOH addition reduced the mobility by approximately 90%. The carrier mobility obtained from the tr-EFM results also decreased by a similar amount upon the addition of NaOH. It is considered that the time evolution of the tr-EFN images reflects the carrier mobility.

4. Conclusion

Tip-synchronized time-resolved EFM based on the pump–probe method was developed using constant-amplitude feedback control, frequency-shift electrostatic force detection, and lock-in detection of the probe pulse train modulation. This method permitted highly sensitive detection of the electrostatic force under a constant tip–sample distance, thereby enabling time-resolved observation of the charge dynamics for the conductive polymer SPAN, which is a relatively poor conductor. Comparison of SPAN thin films with different doping levels revealed the individual differences in carrier density and mobility. The obtained results demonstrate that time-resolved EFM is a powerful tool for elucidating the charge dynamics of hopping conductors such as thermoelectric materials containing metallic grains.

Supporting material

S1: Regarding the shape of the probe pulse; S2: Spatial resolution of tip-synchronized pump–probe EFM; S3: Regarding the temperature dependence of the *I–V* characteristics; S4: Calculations based on the hopping model; S5: Sample topography; S6: Steady-state EFM images; S7: tr-EFM images taken with floating back gate; S8: 2D histograms of the cross-sectional profiles of tr-EFM images of SPAN thin films with NaOH; S9: Estimation of thin-film carrier mobility and carrier density.

Acknowledgment. This work was supported by JSPS KAKENHI Grant Numbers JP25110014, JP24360011, JP16K13667, and 19KK0131.

References

1. Sillin, H. O.; Aguilera, R.; Shieh, H-H.; Avizienis, A. V.; Aono, M.; Stieg, A. Z.; Gimzewski, J. K. A theoretical and experimental study of neuromorphic atomic switch networks for reservoir computing. *Nanotechnology* **2013,** 24, 384004.
2. zur Borg, L.; Domanski, A. L.; Breivogel, A.; Bürger, M.; Berger, R.; Heinze, K.; Zentel, R. Light-induced charge separation in a donor–chromophore–acceptor nanocomposite poly [TPA-Ru(tpy)$_2$] @ZnO. *J. Mater. Chem. C* **2013,** 1, 1223-1230.
3. Gehlen, J. N.; Marchi, M.; Chandler, D. Dynamics affecting the primary charge transfer in photosynthesis. *Science* **1994**, 263, 499-502.
4. Meech, S. R.; Hoff, A. J.; Wiersma, D. A. Role of charge-transfer states in bacterial photosynthesis. *Proc. Natl. Acad. Sci.* **1986,** 83, 9464-9468.
5. Qu, Y.; Duan, X. Progress, challenge and perspective of heterogeneous photocatalysts. *Chem. Soc. Rev.* **2013,** 42, 2568-2580.
6. Hagfeldt, A.; Grätzel, M. Molecular photovoltaics. *Acc. Chem. Res.* **2000,** 33, 269-277.
7. Shockley, W. A unipolar “field-effect” transistor. *Proc. IRE* **1952,** 40, 1365-1376.
8. Manaka, T.; Lim, E.; Tamura, R.; Iwamoto, M. Direct imaging of carrier motion in organic

transistors by optical second-harmonic generation. *Nature Photonics* **2007,** 1, 581-584.

9. Walters, D. A.; Viani, M.; Paloczi, G. T.; Schaeffer, T. E.; Cleveland, J. P.; Wendman, M. A.; Gurley, G.; Elings, V. B.; Hansma, P. K. Atomic force microscopy using small cantilevers, *Proc. Soc. Photo-Opt. Instrum. Eng.* **1997,** 3009, 43–47.
10. Miyata, K.; Tracey, J.; Miyazawa, K.; Haapasilta, V.; Spijker, P.; Kawagoe, Y.; Foster, A. S.; Tsukamoto, K.; Fukuma, T. Dissolution processes at step edges of calcite in water investigated by high-speed frequency modulation atomic force microscopy and simulation. *Nano Lett.* **2017,** 17, 4083-4089.
11. Ando, T.; Uchihashi, T.; Scheuring, S. Filming biomolecular processes by high-speed atomic force microscopy. *Chem. Rev.* **2014,** 114, 3120-3188.
12. Hamers, R. J.; Cahill, D. G. Ultrafast time resolution in scanned probe microscopies. *Appl. Phys. Lett.* **1990,** 57, 2031-2033.
13. Terada, Y.; Aoyama, M.; Kondo, H.; Taninaka, A.; Takeushi, O.; Shigekawa, S. Ultrafast photoinduced carrier dynamics in GaNAs probedusing femtosecond time-resolved scanning tunnelling microscopy. *Nanotechnology* **2007,** 18, 044028.
14. Terada, Y.; Yoshida, S.; Takeuchi, O.; Shigekawa, H. Real-space imaging of transient carrier dynamics by nanoscale pump-probe microscopy. *Nat. Photonics* **2010,** 4, 869-874.
15. Martin, Y.; Abraham, D. W.; Wickramasinghe, H. K. High-resolution capacitance measurement and potentiometry by force microscopy. *Appl. Phys. Lett.* **1988,** 52 1103-1105.
16. Stern, J. E.; Terris, B. D.; Mamin, H. J.; Rugar, D. Deposition and imaging of localized charge on insulator surfaces using a force microscope. *Appl. Phys. Lett.* **1988,** 53, 2717-2719.
17. Miyahara, Y.; Roy-Gobeil, A.; Grutter, P. Quantum state readout of individual quantum dots by electrostatic force detection. *Nanotechnology* **2016,** 28, 064001.
18. Okamoto, K.; Yoshimoto, K.; Sugawara, Y.; Morita, S. KPFM imaging of Si(1 1 1)53×53-Sb surface for atom distinction using NC-AFM. *Appl. Surf. Sci.* **2003,** 210, 128-133.
19. Lochthofen, A.; Mertin, W.; Bacher, G.; Hoeppel, L.; Bader, S.; Off, J.; Hahn, B. Electrical investigation of *V*-defects in GaN using Kelvin probe and conductive atomic force microscopy. *Appl. Phys. Lett.* **2008,** 93, 022107.
20. Sasahara, A.; Pang, C. L.; Onishi, H. Local work function of Pt clusters vacuum-deposited on a TiO_2 surface. *J. Phys. Chem. B* **2006,** 110, 17584-17588.
21. Zhu, J.; Zeng, K.; Lu, L. In-situ nanoscale mapping of surface potential in all-solid-state thin film Li-ion battery using Kelvin probe force microscopy. *J. Appl. Phys.* **2012,** 111, 063723.
22. Yamagishi, Y.; Kobayashi, K.; Noda, K.; Yamada, H. Local carrier dynamics in organic thin film transistors investigated by time-resolved Kelvin probe force microscopy. *Organic Electronics* **2018,** 57, 118-122.
23. Araki, K.; Ie, Y.; Aso, Y.; Matsumoto, T. Fine structures of organic photovoltaic thin films probed

by frequency-shift electrostatic force microscopy. *Jpn. J. Appl. Phys.* **2016,** 55, 070305.

24. Fukuzawa, R.; Takahashi, T. Development of dual bias modulation electrostatic force microscopy for variable frequency measurements of capacitance. *Rev. Sci. Instrum.* **2020,** 91, 023702.
25. Mascaro, A.; Miyahara, Y.; Enright, T.; Dagdeviren, O. E.; Grütter, P. Review of time-resolved non-contact electrostatic force microscopy techniques with applications to ionic transport measurements. *Beilstein J. Nanotechnol.* **2019,** 10, 617-633.
26. Giridharagopal, R.; Rayermann, G. E.; Shao, G.; Moore, D. T.; Reid, O. G.; Tillack, A. F.; Masiello, D. J.; Ginger, D. S. Submicrosecond time resolution Atomic force microscopy for probing nanoscale dynamics. *Nano Lett.* **2012,** 12, 893-898.
27. Karatay, D. U.; Harrison, J. S.; Glaz, M. S.; Giridharagopal, R.; Ginger, D. S. Fast time-resolved electrostatic force microscopy: achieving sub-cycle time resolution. *Rev. Sci. Instrum.* **2016,** 87, 053702.
28. Collins, L.; Ahmadi, M.; Wu, T.; Hu, B.; Kalinin, S. V.; Jesse, S. Breaking the time barrier in Kelvin probe force microscopy: fast free force reconstruction using the G-mode platform. *ACS nano* **2017,** 11, 8717-8729.
29. Schumacher, Z.; Spielhofer, A.; Miyahara, Y.; Grutter, P. The limit of time resolution in frequency modulation atomic force microscopy by a pump-probe approach. *Appl. Phys. Lett.* **2017,** 110, 053111.
30. Jung, W.; Cho, D.; Kim, M.; Choi, M-K. H.; Lyo, I-W. Time-resolved energy transduction in a quantum capacitor. *Proc. Natl Acad. Sci.* **2011,** 108, 13973-13977.
31. Murawski, J.; Mönch, T.; Milde, P.; Hein, M. P.; Nicht, S.; Zerweck-Trogisch, U.; Eng, L. M. Tracking speed bumps in organic field-effect transistors via pump-probe Kelvin-probe force microscopy. *J. Appl. Phys.* **2015,** 118, 244502 (2015).
32. Murawski, J.; Graupner, T.; Milde, P.; Raupach, R.; Zerweck-Trogisch, U.; Eng, L. M. Pump-probe Kelvin-probe force microscopy: principle of operation and resolution limits. *J. Appl. Phys.* **2015,** 118, 154302.
33. Matsumoto, T.; Kawai, T. Time-resolved electrostatic force detection using scanning probe microscope. *Microscopy* **2008,** 43, 149-151.
34. Dwyer, R. P.; Nathan, S. R.; Marohn, J. A. Microsecond photocapacitance transients observed using a charged microcantilever as a gated mechanical integrator. *Sci. Adv.* **2017,** 3, e1602951.
35. Araki, K.; Ie, Y.; Aso, Y.; Ohoyama, H.; Matsumoto, T. Time-resolved electrostatic force microscopy using tip-synchronized charge generation with pulsed laser excitation. *Commun. Phys.* **2019,** 2, 10.
36. Kang, S. D.; Snyder, G. J. Charge-transport model for conducting polymers. *Nature Materials* **2017,** 16, 252-257.
37. Wei, X.-L.; Wang, Y. Z.; Long, S. M.; Bobeczko, C.; Epstein, A. J. Synthesis and Physical

Properties of Highly Sulfonated Polyaniline. *J. Am. Chem. Soc.* **1996,** 118, 2545-2555.

38. Strounina, E. V.; Shepherd, R.; Kane-Maguire, L. A. P.; Wallace, G. G. Conformational changes in sulfonated polyaniline caused by metal salts and OH^-. *Synthetic Metals.* **2003,** 135-136, 289-290.
39. Asadi, K.; Kronemeijer, A.; Cramer, T.; Jan Anton Koster, L.; Blom, P. W. M.; de Leeuw, D. M. Polaron hopping mediated by nuclear tunnelling in semiconducting polymers at high carrier density. *Nat. Commun.* **2013,** 4, 1710.

Scheme 1.

Molecular structure of sulfonated polyaniline (SPAN).

Figure 1. (a) UV–vis absorption spectra of SPAN solutions with NaOH concentrations ranging from 0 to 1.0×10^{-3} M. (b) *I–V* plots of SPAN films prepared from 5×10^{-3} wt% SPAN solution (blue line) and 5×10^{-3} wt% SPAN solution containing 1.0×10^{-4} M NaOH (orange line).

Figure 2. Schematic diagram of the tip-synchronized pump–probe tr-EFM apparatus. The cantilever is vibrated by self-excitation at its resonant frequency. The pump–probe sequence is triggered by the photodiode output signal. The frequency shift is monitored by the PLL to measure the attractive force reflecting the electrostatic force between the tip and sample. SPM scanning is performed in the constant-amplitude feedback mode to maintain a constant tip–sample distance. The PLL output is detected by the lock-in amplifier with the on/off modulation of the probe pulse train as the reference signal.

Figure 3. Timing chart for the tip-synchronized pump–probe tr-EFM measurements. The trigger signal is generated by the cantilever vibration. The pump pulse V_d applied to the drain electrode is controlled to be an integer multiple of the cantilever oscillation period to avoid interference between the pump pulse and tip motion. The probe pulse V_t applied to the tip is locked at the moment when the tip reaches its closest position to the sample surface. The pump pulse and probe pulse are periodically applied to the drain electrode and cantilever, respectively. The period is approximately 22 μs, which is the mean duration between a certain probe (pump) pulse and the subsequent probe (pump) pulse. The delay between the pump and probe pulses is controlled by a trigger signal before one cycle of cantilever oscillation. On/off modulation of the probe pulse train is employed for lock-in detection of the PLL output.

Figure 4.

(a) Variation of the frequency shift as a function of the phase delay between tip vibration and the probe pulse for a Au surface using a DC sample voltage of $V_s = -4$ V and a probe pulse of $V_t = 4$ V. (b) Comparison of the frequency shift variation with and without synchronization of the probe pulse to the tip motion. The shaded region indicates periodic application of a sample bias of $V_s = -4$ V and the non-shaded region a sample with $V_s = 0$ V. The frequency shift variation was larger with tip synchronization. Error bars indicate the maximum or minimum value as appropriate.

Figure 5. Pump–probe tr-EFM images of SPAN thin films. (a) Topography of the SPAN thin film showing the drain and source electrodes. The image was acquired simultaneously with the tr-EFM images. (b) tr-EFM images obtained 0.3, 5.0, and 9.5 μs after turning on the pump bias of $V_d = -2$ V and their averaged cross-sectional profiles (each profile is the average of 124 scan lines). (c) tr-EFM images obtained in the ON state

and 0.7, 1.7, and 9.7 μs after turning off the pump bias and their averaged cross-sectional profiles (each profile is the average of 124 scan lines). The time axis and graphics to the right side of (b) and (c) show the timing of the probe pulse for each tr-EFM image to pump pulse. The green hatched area and white area of the axis indicate the ON and OFF states, respectively. Vertical lines on the time axis indicate the duration of the probe pulse used to obtain each tr-EFM image. The timing of probe pulse *t* is shown at the top right of each image.

Figure 6.

Calculated time evolution of the product of the carrier density and potential of the thin films as a function of the position between the source and drain electrodes for the processes of (a) charge injection and (b) discharge using the hopping model.

Figure 7. Pump–probe tr-EFM images of SPAN thin films with and without NaOH. (a) tr-EFM images of SPAN thin film without NaOH taken in the ON state, 0.7 and 9.7 μs after turning off the pump bias, and immediately after turning on the pump bias of $V_d = -2$ V again, and their averaged cross-sectional profiles (each profile is the average of 124 scan lines). (b) tr-EFM images of SPAN thin film with NaOH taken in the ON state, 0.7 and 10.7 μs after turning off the pump bias, and immediately after turning on the pump bias of $V_d = -2$ V again, and their averaged cross-sectional profiles (each profile is the average of 200 scan lines). The time axis and graphics between (a) and (b) show the timing of the probe pulse for each tr-EFM image to pump pulse. The green hatched area and white area of the axis indicate the ON and OFF states, respectively. Vertical lines on the time axis indicate the duration of the probe pulse used to obtain each tr-EFM image. The timing of probe pulse *t* is shown at the top right of each image.

393 TOC graphic

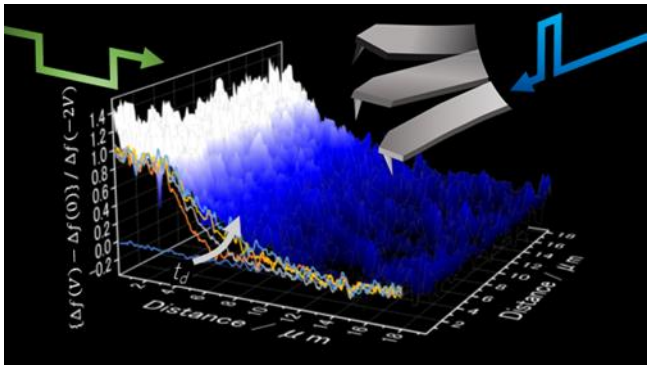

394